Instabilities of the Sidewall Boundary Layer in a Rapidly Rotating Split Cylinder

J. M. Lopez and P. Gutierrez

School of Mathematical and Statistical Sciences
Arizona State University, Tempe AZ 85287, USA

Abstract

The instabilities of the sidewall boundary layer in a rapidly rotating split cylinder are studied numerically. Axisymmetric results are studied extensively where a variety of different states are found. In the basic state, the interior flow is in solid-body rotation with the mean rotation rate of the two cylinder halves. The sidewall boundary layer of the basic state is compared with theoretical results. For sufficiently fast mean rotation and large enough differential rotation between the two halves, instabilities in the boundary layer appear. These instabilities result in periodic and quasi-periodic states in different parameter regimes. The instabilities are localized in the boundary layer, but they may transport shear into interior if their associated frequencies are less than twice the mean rotation frequency, and then only in the form of inertial wave beams along directions determined by the frequencies.

Introduction

The structure of the sidewall boundary layer in a rapidly rotating cylinder subjected to some differential rotation has attracted much attention because of both its practical and fundamental importance. Stewartson [8] showed that when the sidewall rotates at a rate slightly faster than the two endwalls, the sidewall boundary layer has a sandwich structure consisting of an inner layer whose thickness scales as $Re^{-1/3}$ (where Re is the rotation Reynolds number based on the mean angular velocity of the cylinder, its radius and the kinetic viscosity of the fluid) and an outer layer with a thickness that scales as $Re^{-1/4}$. The $Re^{-1/4}$ layer is where the perturbation to the azimuthal velocity is adjusted and the inner $Re^{-1/3}$ layer is needed to adjust the secondary meridional flow. The boundary layers on the endwalls are of Ekman type, and scale as $Re^{-1/2}$.

Hocking [3] considered another differentially rotating cylinder flow consisting of a split cylinder with one half rotating slightly faster than the other. His analysis considered the case of an infinitely long cylinder in which case the meridional flow in the sidewall layer due to the flows being pumped out of the Ekman layers at the ends was negligible. The finite split cylinder problem was later addressed by van Heijst [9] who conducted the boundary layer analysis in a finite fully enclosed split cylinder, showing that in the limit of small differential rotation, the $Re^{-1/4}$ layer is where the interior flow adjusts to the sidewall, and the jump discontinuity due to the split in the cylinder is accounted for in the inner $Re^{-1/3}$ layer. From a linear boundary layer analysis perspective, where the split in the finite enclosed cylinder occurs determines what roles the $Re^{-1/3}$ and $Re^{-1/4}$ layers play. Van Heijst [9] showed that if the split is at half height, then the $Re^{-1/3}$ provides the matching of the interior flow to the discontinuous sidewall boundary condition as well as accounting for the induced meridional flow, and that the $Re^{-1/4}$ layer is absent. On the other hand, if the split is at one of the corners where an endwall meets the sidewall, then the $Re^{-1/3}$ layer is absent and the matching is completely accomplished by the $Re^{-1/4}$ layer.

The theoretical boundary layer analysis aims to describe the steady axisymmetric basic state, and this is done in the limit of very small differential rotation so that the equations can be linearized about the state of solid-body rotation. Of course, this raises the question as to what happens as the differential rotation is increased; how does the flow lose stability and transition to turbulence? Hart and Kittelman [2] provide some insights from flow visualization experiments in the case where the rapidly rotating cylinder has the top endwall rotating faster. Lopez [4] simulated this and other related flows solving the axisymmetric Navier–Stokes equations, but subsequently it was shown [5] that the primary instabilities are three-dimensional in nature. Is this also the case when the split is at the cylinder half height? Here, we not only focus on the nature of the primary instabilities of the split cylinder flow, but also address how these instabilities, which are associated with both the sidewall boundary layer flow and the corner flow in the slow half cylinder (which is not analytically amenable), affect the interior flow.

For these rapidly rotating split cylinder problems, in the absence of instabilities the interior flow is in solid-body rotation with the mean rotation rate of the two cylinder halves. For fast enough mean rotation, disturbances from instabilities can only penetrate into the interior if their frequencies are less than twice the mean rotation frequency, and then only in the form of inertial wave beams along directions determined by the frequencies. In the inviscid limit, this is governed by the inertial wave dispersion relation [1], but for large but finite Re and finite differential rotation, viscous and nonlinear effects come into play, as well as mean-flow deformations leading to bulk flows that have non-constant angular speed. Furthermore, how these inertial wave beams feed back on the boundary layer and corner instabilities is not obvious, and we try to address this.

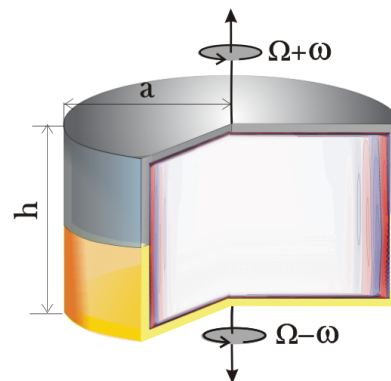### Governing Equations and Numerical Methods

Figure 1: Schematic of the flow system. The inset shows azimuthal vorticity contours of an axisymmetric time-periodic state at $Re = 10^5$, $Ro = 0.110$ and $\gamma = 1$.

Consider the flow in a circular cylinder of radius a and height h, completely filled with a fluid of kinematic viscosity ν. The cylinder is split in two, the top half rotates with angular speed
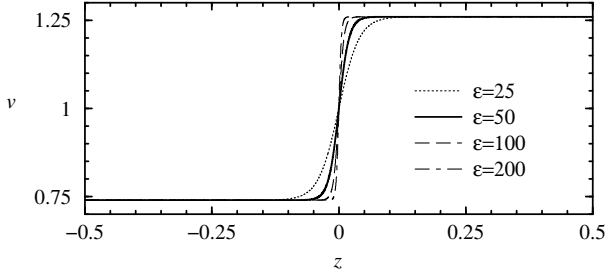
Figure 2: Profiles of the regularized sidewall boundary condition for the azimuthal velocity, $v(z) = 1 + Ro \tanh(\varepsilon z)$, with $Ro = 0.26$ and ε as indicated.

$\Omega + \omega$ and the bottom half with angular speed $\Omega - \omega$. Figure 1 shows a schematic of the flow.

The Navier–Stokes equations, non-dimensionalized using a as the length scale and $1/\Omega$ as the time scale, are

$$(\partial_t + \boldsymbol{u} \cdot \nabla)\boldsymbol{u} = -\nabla p + 1/Re\nabla^2 \boldsymbol{u}, \qquad \nabla \cdot \boldsymbol{u} = 0, \quad (1)$$

where $\boldsymbol{u} = (u, v, w)$ is the velocity field in polar coordinates $(r, \theta, z) \in [0,1] \times [0, 2\pi] \times [-\gamma/2, \gamma/2]$, and p is the kinematic pressure. There are three governing parameters:

$$\begin{aligned}
&\text{Reynolds number} &&Re = \Omega a^2/\nu,\\
&\text{Rossby number} &&Ro = \omega/\Omega, &&(2)\\
&\text{aspect ratio} &&\gamma = a/h.
\end{aligned}$$

The boundary conditions are no-slip:

$$\begin{aligned}
z = 0.5\gamma: &\quad (u,v,w) = (0, r(1+Ro), 0),\\
z = -0.5\gamma: &\quad (u,v,w) = (0, r(1-Ro), 0),\\
r = 1, z \in (0, 0.5\gamma): &\quad (u,v,w) = (0, 1+Ro, 0),\\
r = 1, z \in (0, -0.5\gamma): &\quad (u,v,w) = (0, 1-Ro, 0).
\end{aligned} \quad (3)$$

The governing equations (1) have been solved using a second-order time-splitting method, with space discretized via a Galerkin–Fourier expansion in θ and Chebyshev collocation in r and z:

$$\boldsymbol{u}(r, \theta, z, t) = \sum_{n=0}^{2n_r+1} \sum_{m=0}^{n_z} \sum_{k=-n_\theta/2}^{k=n_\theta/2-1} \hat{\boldsymbol{u}}_{mnk}(t) \Xi_n(r) \Xi_m(z) e^{ik\theta}, \quad (4)$$

where Ξ_n is the n-th Chebyshev polynomial. The spectral solver is based on that described in Ref. [7] and it has been used extensively in a wide variety of enclosed cylinder flows.

The jump discontinuity in the sidewall boundary condition for the azimuthal velocity is problematic when solving the system using a spectral method as it leads to Gibb's phenomenon. This can be remedied by regularizing the boundary condition by smoothing out the jump over a small distance, in essentially the same way as the corner discontinuity between a sidewall and a differentially rotating endwall is regularized [6]. Specifically, we replace the boundary condition for the azimuthal velocity with

$$v(r=1, \theta, z) = 1 + Ro \tanh(\varepsilon z), \quad (5)$$

where ε governs the distance over which the jump is smooth out. Figure 2 shows the azimuthal velocity profile at the sidewall for $Ro = 0.26$ and various values of ε. Figure 3 shows the azimuthal vorticity for $Re = 10^4$, $Ro = 0.26$, $\gamma = 1$ with $\varepsilon = 50$ and $\varepsilon = 200$. There is little difference in selecting $\varepsilon > 50$, and for the rest of the results presented here, we fix $\varepsilon = 50$.
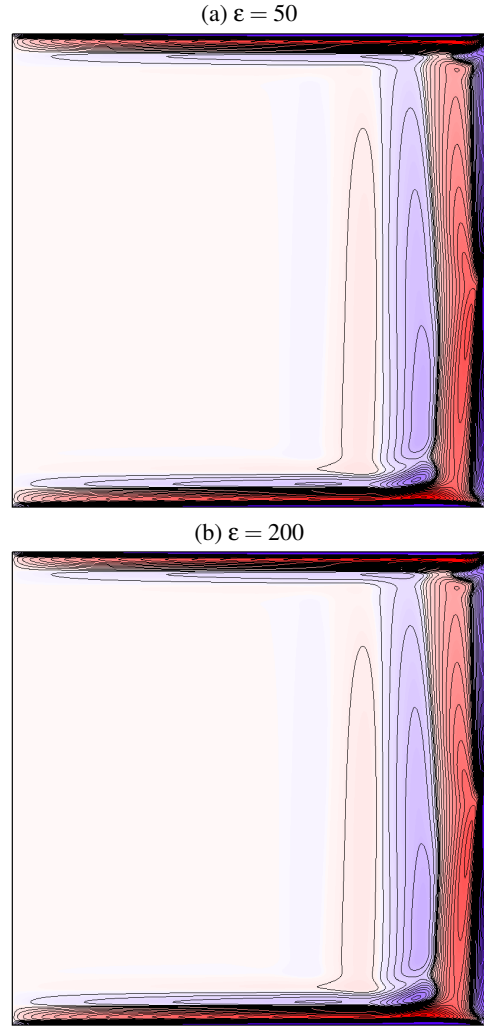

Figure 3: Contours of the azimuthal vorticity η of the basic state at $Re = 10^4$, $Ro = 0.26$, $\gamma = 1$ and two values of ε. There are 20 positive (red) and 20 negative (blue) contours that are quadratically spaced in the range $\eta \in [-5, 5]$.

A global quantitative measure of the flow is provided the kinetic energy of the solution. In general, the modal kinetic energy of the Fourier modes corresponding to azimuthal wavenumber m are

$$E_m = 0.5 \int_{-0.5\gamma}^{0.5\gamma} \int_0^1 \boldsymbol{u}_m \cdot \boldsymbol{u}_m^* r \, dr \, dz, \quad (6)$$

where $\boldsymbol{u}_m$ is the mth Fourier mode of the velocity field and $\boldsymbol{u}_m^*$ is its complex conjugate. For axisymmetric states, only E_0 is non-zero.

Sidewall Boundary Layer Structure

In the basic state, BS, the interior flow is in solid-body rotation with approximately the mean rotation rate of the two cylinder halves when Ro is small. In this section we examine how the basic state varies with Ro, Re and γ.

Van Heijst [9] used boundary layer analysis to solved the shear-layer structure of a finite cylinder split in two differentially rotating parts. The main effect of including the two lids is the order $(Re^{-1/2})$ transport that appears in the Stewartson layer coming from the respective Ekman layers. He described how the combination of the $Re^{-1/4}$ and $Re^{-1/3}$ boundary layers match the boundary conditions. For the case we study here, with the
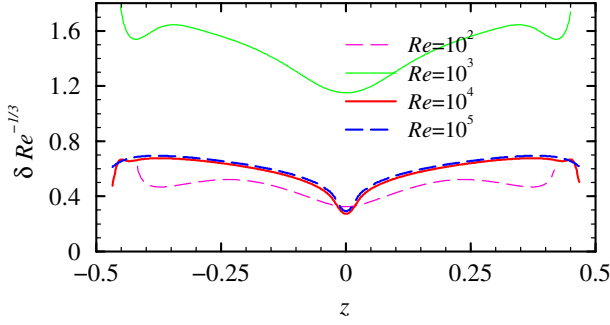
Figure 4: Scaled sidewall boundary layer thickness, $\delta Re^{-1/3}$ along the length of the cylinder for $Ro = 10^{-5}$ and $\gamma = 1$.

discontinuity in the middle of the cylinder, only the zero field of the $Re^{-1/3}$ appears and the $Re^{-1/4}$ layer is absent. All the boundary layer analysis results were obtained in the $Ro \to 0$ limit and neglecting curvature and inertia.

In our simulations, the Reynolds number is finite, but we consider Re as large as 10^5. Figure 4 shows the sidewall boundary layer thickness from our simulations. This boundary layer thickness, $\delta(z)$, is determined as the radial distance from the sidewall where the azimuthal vorticity first changes sign. The results in the figure correspond to $\gamma = 1$ and $Ro = 10^{-5}$. The value of γ is not qualitatively very important, but Ro needs to be small in order to approach the asymptotic regime considered in the boundary layer analysis. The figure plots $\delta(z)Re^{-1/3}$, and shows that the asymptotic scaling is achieved for $Re \gtrsim 10^4$.

The Rossby number affects the velocity profile and boundary layer thickness. For $Ro < 0.001$, the flows are almost reflection symmetric about the half-height (perfect reflection symmetry is only present at $Ro = 0$). For these low Ro cases, the flow is centrifuged radially outward from the top and bottom endwall layers and continue from the corners towards the half-height forming the sidewall boundary layer. The outflow from the faster rotating (top) endwall is stronger, and so there is a slight overshoot in the top-half sidewall boundary layer flow past the cylinder split at half-height when Ro is small. For $Ro \gtrsim 10^{-3}$, this overshoot leads to departures from the $Ro \ll 1$ analysis and the flow is significantly different. In particular, the basic state loses stability in a variety of ways, and the bottom corner region which is analytically inaccessible becomes dynamically important as the flow from the upper half of the sidewall boundary layer reaches it.

Axisymmetric Instabilities of the Sidewall Layer

The regime diagram, figure 5, shows the loci of different solutions in (Ro, γ)-parameter space for $Re = 10^5$. For small Ro and γ, the basic state is stable and it loses stability to two different time-dependent states, LC1 and LC2, as either Ro or γ are increased. For larger γ and smaller Ro, there is a supercritical Hopf bifurcation to the limit cycle LC1 with frequency ω_1, whereas for larger Ro and smaller γ, there is a different supercritical Hopf bifurcation to the limit cycle LC2 with frequency ω_2. At about $Ro = 0.8$ and $\gamma = 0.6$, there is a point where the two Hopf bifurcations occur simultaneously, and as is typical in double Hopf bifurcations, there is a region of parameter space anchored at the double-Hopf point and delimited by Neimark-Sacker bifurcation curves where a mixed mode exists. Since ω_1 and ω_2 are generically incommensurate, the mixed mode QP is quasi-periodic. The regime diagram also includes regions further removed from the double-Hopf point where QP has undergone a pair of period-doubling bifurcations to states QP2 and
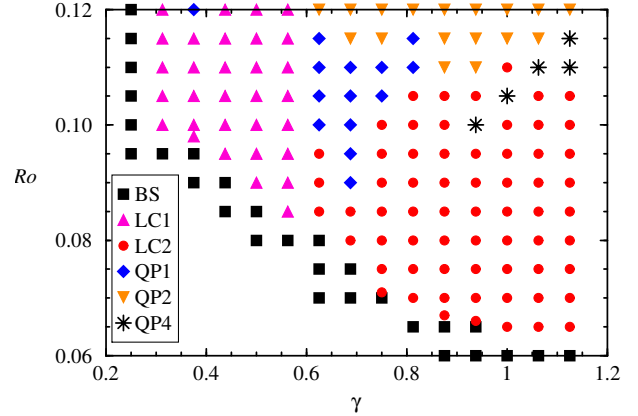

Figure 5: Regime diagram in (Ro, γ)-space, showing the various axisymmetric states found near the double Hopf bifurcation for $Re = 10^5$.

QP4.

The oscillations in LC1 are localized at the bottom corner where the sidewall and bottom endwall meet. There is a periodic swelling of the sidewall boundary layer near the corner, as can be seen in a snap-shot of the azimuthal vorticity at $Re = 10^5$, $Ro = 0.11$ and $\gamma = 0.5$ shown in figure 6(a). The frequency $\omega_1 \approx 1.88$. Linear inviscid theory for rapidly rotating flow [1] gives that inertial waves can be generated in rapidly rotating flows if the perturbation frequency is less than twice the angular speed Ω of the flow. Since we non-dimensional time with Ω, disturbance frequencies less than two are expected to generate inertial waves, and these should obey the dispersion relation giving the angle at which they propagate with respect to the rotation axis as $\alpha = \arccos(\omega_{\text{disturbance}}/2)$. For $\omega_{\text{disturbance}} = \omega_1 \approx 1.88$, this gives that the inertial wave beams should propagate into the bulk at an angle $\alpha_1 \approx 20°$, emanating from the bottom corner region where the periodic disturbance associated with the Hopf bifurcation is localized. Indeed, figure 6(a) shows such inertial waves.

The LC2 state is very different to LC1. To begin with, the oscillations are localized in the deep sidewall boundary layer just below the split at half-height. They consist of a periodic train of roll vortices traveling down the sidewall all the way to the bottom corner. Furthermore, the frequency associated with this oscillation is $\omega_2 \approx 4.23$, which is too high to generate inertial waves in the interior, which continues to rotate as an essentially solid body, as in the basic state BS. Figure 6(b) shows that all the azimuthal vorticity is contained inside the top and bottom Ekman layers and in the sidewall layer, and the LC2 downward traveling rollers in the deep sidewall layer are clearly evident.

For the quasiperiodic state QP, found after crossing either of the Neimark-Sacker bifurcation curves, figure 6(c) illustrates the behavior of the mixed mode. The instabilities are present in the bottom half of the sidewall as in LC2 superposed with the instability in the corner resulting from LC1 that drives inertial waves. A power spectral density of the time-series of E_0 for QP comprises of strong peaks at frequencies ω_1 and ω_2 (their relative strength depend on the distance in (Ro, γ)-space the QP case under consideration is from the two Neimark-Sacker curves), and their linear combinations. The peaks at the linear combinations are weaker than the peaks at ω_1 and ω_2, but there can be several peaks at frequencies $m\omega_1 + n\omega_2 < 2$ (m and n integers) and if they are sufficiently strong, they can also generate inertial waves at angles $\arccos(m\omega_1 + n\omega_2)/2$. For the example shown in figure 6(c), these other frequencies are too weak and the related inertial waves are negligible compared to the inertial
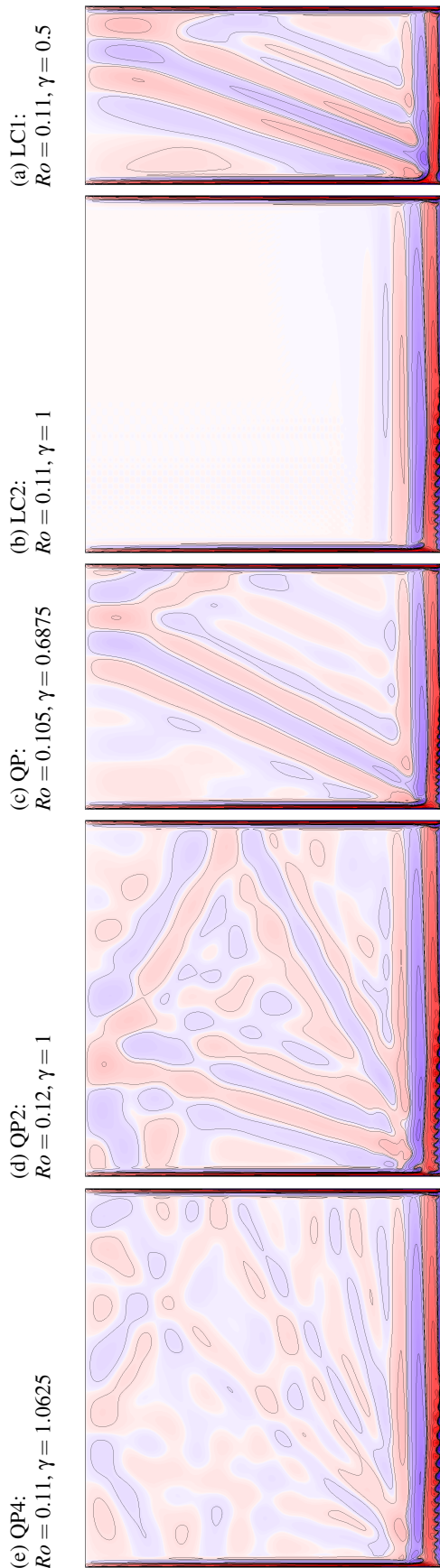
(a) LC1: $Ro = 0.11$, $\gamma = 0.5$

(b) LC2: $Ro = 0.11$, $\gamma = 1$

(c) QP: $Ro = 0.105$, $\gamma = 0.6875$

(d) QP2: $Ro = 0.12$, $\gamma = 1$

(e) QP4: $Ro = 0.11$, $\gamma = 1.0625$

Figure 6: Snapshots of η at $Re = 10^5$ and Ro and γ as indicated. Ten cubically spaced contour levels are in the range $\eta \in [-5, 5]$.

wave generated by the peak at ω_1. Note that the frequencies ω_1 and ω_2 are (weak) functions of Ro and γ, and so the angle of the inertial wave in figure 6(c) differs from that in figure 6(a). The dependence of ω_1 and ω_2 on Ro and γ can lead to low order frequency lockings and with combinations $m\omega_1 + n\omega_2$ that gives strong peaks at subharmonics of ω_1. This seems to be the case with QP2 and QP4 which have strong peaks at frequencies $\omega_1/2$ and $\omega_1/4$, respectively. Figure 6(d) shows a snap-shot of azimuthal vorticity of a QP2 case, with an inertial beam generated by ω_1 with angle $\alpha \approx 20°$, very similar to the QP case in figure 6(c), and another beam at angle $\alpha \approx 62°$ corresponding to the peak at $\omega_1/2$. The QP4 case shown in figure 6(e) has an even more complicated inertial wave structure, but one can decipher beams at about $20°$, $45°$, $62°$ and $76°$, but they are not as clean as in the other cases, probably due to interference between the beams and their reflections, and well as further contributions from other linear combinations of frequencies.

Conclusions

The simulations of a rapidly differentially rotating split cylinder flow have identified a number of instabilities of the sidewall boundary layer, and some of these are able to transport shear throughout the whole cylinder, overcoming the Taylor-Proudman constraint if the frequencies associated with the instabilities are less than twice the mean rotation frequency. Future investigations shall examine the role of three-dimensional perturbations.

Acknowledgements

References

[1] Greenspan, H. P., *The Theory of Rotating Fluids*, Cambridge University Press, 1968.

[2] Hart, J. E. and Kittelman, S., Instabilities of the sidewall boundary layer in a differentially driven rotating cylinder, *Phys. Fluids*, **8**, 1996, 692–696.

[3] Hocking, L. M., An almost-inviscid geostrophic flow, *J. Fluid Mech.*, **12**, 1962, 129–134.

[4] Lopez, J. M., Characteristics of endwall and sidewall boundary layers in a rotating cylinder with a differentially rotating endwall, *J. Fluid Mech.*, **359**, 1998, 49–79.

[5] Lopez, J. M. and Marques, F., Sidewall boundary layer instabilities in a rapidly rotating cylinder driven by a differentially co-rotating lid, *Phys. Fluids*, **22**, 2010, 114109.

[6] Lopez, J. M. and Shen, J., An efficient spectral-projection method for the Navier-Stokes equations in cylindrical geometries I. Axisymmetric cases, *J. Comput. Phys.*, **139**, 1998, 308–326.

[7] Mercader, I., Batiste, O. and Alonso, A., An efficient spectral code for incompressible flows in cylindrical geometries, *Computers & Fluids*, **39**, 2010, 215–224.

[8] Stewartson, K., On almost rigid rotations, *J. Fluid Mech.*, **3**, 1957, 17–26.

[9] van Heijst, G. J. F., The shear-layer structure in a rotating fluid near a differentially rotating sidewall, *J. Fluid Mech.*, **130**, 1983, 1–12.